ACS APPLIED MATERIALS & INTERFACES

www.acsami.org

Research Article

Highly Efficient HTM-Free Tin Perovskite Solar Cells with Outstanding Stability Exceeding 10000 h

Parameswaran Rajamanickam, Sudhakar Narra, Ashank Seetharaman, and Eric Wei-Guang Diau*

Cite This: *ACS Appl. Mater. Interfaces* 2023, 15, 40700−40708

Read Online

ACCESS | Metrics & More | Article Recommendations | Supporting Information

ABSTRACT: The bottleneck in the rapid development of tin-based perovskite solar cells (TPSCs) is the inherent chemical instability. Although this is being addressed continuously, the device performance has not improved further due to the use of PEDOT:PSS as the hole-transport material (HTM), which has poor long-term stability. Herein we have applied commercial ITO nanoparticles over ITO glass substrates and altered the surface chemistry of the ITO electrode via a simple two-step thermal annealing, followed by a UV−ozone treatment. These surface-modified ITO electrodes display promising interfacial characteristics, such as a suitable band alignment owing to significantly reduced surface carbon contamination, increased In−O bonding, and reduced oxygen vacancies, that enabled fabrication of an HTM-free TPSC device according to a two-step method. The fabricated device possessed an outstanding power conversion efficiency (PCE) of 9.7%, along with a superior long-term stability by retaining over 90% of the initial PCE upon shelf storage in a glovebox for a period of over 10000 h. The application of ITO nanoparticles led to effective interfacial passivation, whose impacts on the long-term durability were assessed using electrochemical impedance spectroscopy, time-resolved photoluminescence decay profiles, and femtosecond transient absorption spectroscopy techniques.

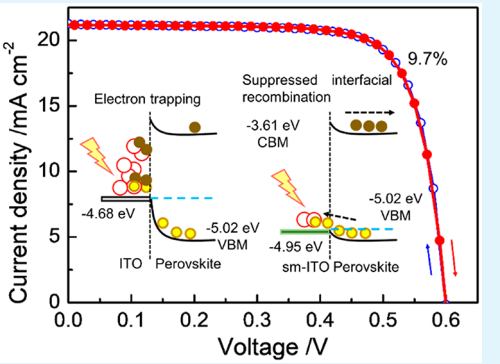

KEYWORDS: *tin perovskites, interfacial engineering, surface modification, two-step sequential deposition, HTM-free tin perovskite solar cells, long-term stability*

INTRODUCTION

Persistent efforts toward addressing the chemical instability issues have led to the recent rapid development in nontoxic lead-free tin-based perovskite solar cells (TPSCs).[1,2] For instance, formamidinium (FA) as an alternative to methylammonium (MA),[3−5] additive and coadditive incorporation,[6−13] and 3D/2D hybrid structures[14−17] have been reported. Furthermore, the inverted p-i-n planar device configuration is being widely adopted to circumvent the unfavorable charge carrier transport in TPSCs.[2] In this regard, the hole extraction at the hole transport layer/perovskite (HTL/PSK) interface is generally enabled by using poly(3,4-ethylenedioxythiophene):poly(styrenesulfonate) (PEDOT:PSS) as the HTL.[18,19] Although PEDOT:PSS is a promising hole transport material (HTM) for solar cell applications, its effects of high acidity, hygroscopicity, anisotropic carrier injection, and photothermal vulnerability outweigh its attractive characteristics with a poor longer-term stability, thus suppressing the device performance.[20] While poly(triaryl)amine (PTAA) can replace PEDOT:PSS, the high hydrophobic nature of the former prevents uniform perovskite film formation, thus demanding additional pretreatment using a phenethylammonium iodide (PEAI) interlayer.[21] Nevertheless, the incorporation of organic PTAA and PEAI would still lead to thermal stress after prolonged use.[22] Hence, it becomes essential to develop stable alternative HTMs[23] or a device without involving HTL.[24,25]

The first attempt to fabricate HTM-free TPSC yielded a low power conversion efficiency (PCE) of 3.7% as a result of inappropriate energy-band alignment of the perovskite with the ITO electrodes and poor film formation.[26] A later work focused on the energy-level alignment by applying a 2D/3D heterojunction and obtained a decent device performance with a PCE of 5.2% in a HTM-free TPSC.[27] Furthermore, Han and co-workers reported an HTM-free TPSC by doping ammonium cation salt ($EDAI_2$) as the nuclear sites for appropriate band alignment to attain a PCE of 10.1% with good thermal and light-soaking stability.[28] Subsequently, more emphasis was given to interfacial modification[29] via simple dip-coating of self-assembled hole-selective monolayers to functionalize the ITO substrates.[24,25] The functionalization

Received: July 17, 2023
Accepted: August 7, 2023
Published: August 17, 2023

https://doi.org/10.1021/acsami.3c10268
ACS Appl. Mater. Interfaces 2023, 15, 40700−40708

was accomplished by tuning the surface properties of the underlying transparent electrodes via facile thermal annealing that improved the interfacial properties.[30]

In this work, we have incorporated ITO nanoparticles on an ITO glass substrate to provide adequate nucleation sites for the growth of perovskite grains and applied two-step thermal annealing to manipulate the surface chemistry of the ITO layer. The resulting transparent electrode possessed appropriate optical and charge-transport characteristics to enable the fabrication of an HTM-free TPSC with an excellent PCE of 9.7%. The applied inorganic metal oxide nanoparticles activate the ITO surface to get rid of undesired excess carbon contamination from the substrate, while the subsequent thermal annealing repairs the surface, leading to a suitable band alignment, smooth perovskite film formation, and effective interfacial passivation, due to which the devices possessed an impressive enduring stability of over 10000 h upon shelf storage in a glovebox, thus competing with the traditional HTM-based TPSCs.

RESULTS AND DISCUSSION

The schematic representation of the surface modification of ITO (sm-ITO) glass along with the device fabrication process is shown in Figure 1. The surface modification was performed

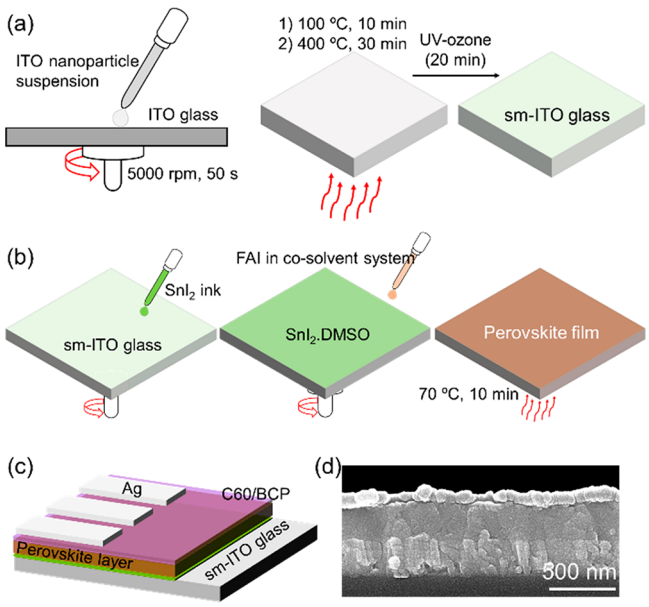

Figure 1. (a) Schematic illustration of the development of sm-ITO electrodes using ITO nanoparticle coating and annealing as indicated. (b) Scheme for the two-step sequential deposition method using a cosolvent approach. (c) Full device architecture in the inverted planar p-i-n configuration. (d) Cross-sectional SEM image of the fabricated device using sm-ITO displaying no visible nanoparticulate interlayer.

by dispersing commercial ITO nanoparticles (In_2O_3:SnO_2 = 90:10, 20−70 nm) in dry-distilled ethanol and spin-coating them onto the ITO glass substrates, followed by annealing in an oxygen atmosphere (Figure 1a). The surface morphology of the resulting sm-ITO electrodes looks almost indistinguishable from the conventional ITO substrate, although a subtle improvement in smoothness can be seen with reduced microcrack-like features (Figure S1a,b). The cross-sectional features (Figure S1c,d) indicate that the surface treatment did not alter the ITO thickness. Moreover, no visibly separate interlayer between ITO and perovskite can be seen in the sm-ITO. When probed using AFM, the surface characteristics of bare ITO look almost identical with those of sm-ITO, except with a slightly lower rms (Figure S2), agreeing with the SEM image of reduced microcrack-like features. Although this change looks insignificant, this subtle alteration leads to significant changes in the wettability of the sm-ITO. We measured the contact angle for the substrates using the perovskite precursor solutions (Figure S3) and found that the sm-ITO has the smallest (nearly zero) contact angle in comparison to that of PEDOT:PSS film deposited on ITO due to the altered surface energy, polarity, and hardness that yielded better surface features.[31,32] A two-step sequential deposition approach involving a cosolvent system[33] was adopted to form the perovskite thin films atop the transparent sm-ITO electrodes (Figure 1b). The improved surface features of the ITO substrates enabled a smooth spread of the SnI_2 precursor solution, thus facilitating a uniform pinhole-free perovskite layer having a better interaction with the electrode surface (Figure S4). The two-step approach is known to inhibit the rapid crystallization associated with tin perovskites through the careful selection of mixed solvents and the delayed FAI injection over an already formed SnI_2·3DMSO complex.[34] Figure 1c displays the device architecture in the inverted planar p-i-n configuration (sm-ITO/($FASnI_3$+1% $EDAI_2$)/C60/BCP/Ag), and Figure 1d shows the cross-sectional SEM image of the device fabricated in this work. There is no visible presence of a separate nanoparticulate interlayer between the sm-ITO electrode and the perovskite active layer, implying that the nanoparticles did not form a layer to cover the ITO substrate; instead, they may have induced chemical changes.

To understand the chemical component variation due to the surface modification process, we performed XPS studies on the references ITO-UVO (UV−ozone-treated for 20 min), ITO-400 (annealed to 400 °C for 30 min), and sm-ITO; the corresponding results are shown in Figure S5. To compare the effects of annealing and UVO treatments, we also performed XPS measurements for the bare ITO substrate and ITO nanoparticles without any post-treatments. The amounts in atom % of In, Sn, and O and residual surface carbon in these ITO electrodes and nanoparticles are given in Table S1. According to the XPS results, the major components of the electrodes are In, O, and C, while the amount of Sn is substantially low and remained almost unchanged after surface modification. Hence, we focused our discussions on C, In, and O. The recorded XPS spectra were deconvoluted to get a better understanding of the ITO surface chemistry. The C 1s spectra of all the substrates possessed the characteristic C−C, C−O−C, and O−C═O peaks (Figure S5a),[35] with the total amount of carbon being found to be significantly lower in sm-ITO (16.6 atom %) than the others (Table S1). Although UV−ozone treatment can slightly reduce the surface carbon contamination and induce surface energy changes on the ITO,[36] we found that annealing had a greater impact on them, while sm-ITO was able to display superior characteristics in terms of purity induced by the nanoparticle treatment prior to the thermal annealing process. The O 1s spectra comprise the surface oxides (M−O), oxygen vacancies (V_O), and surface hydroxyls (M−OH) (Figure S5b). The intensity associated with M−O was seen to increase for ITO-400 and sm-ITO, while those of V_O and M−OH diminished significantly in comparison to the bare ITO, which can be attributed to oxidation due to annealing.[37,38] The sm-ITO has a slightly

https://doi.org/10.1021/acsami.3c10268
ACS Appl. Mater. Interfaces 2023, 15, 40700−40708

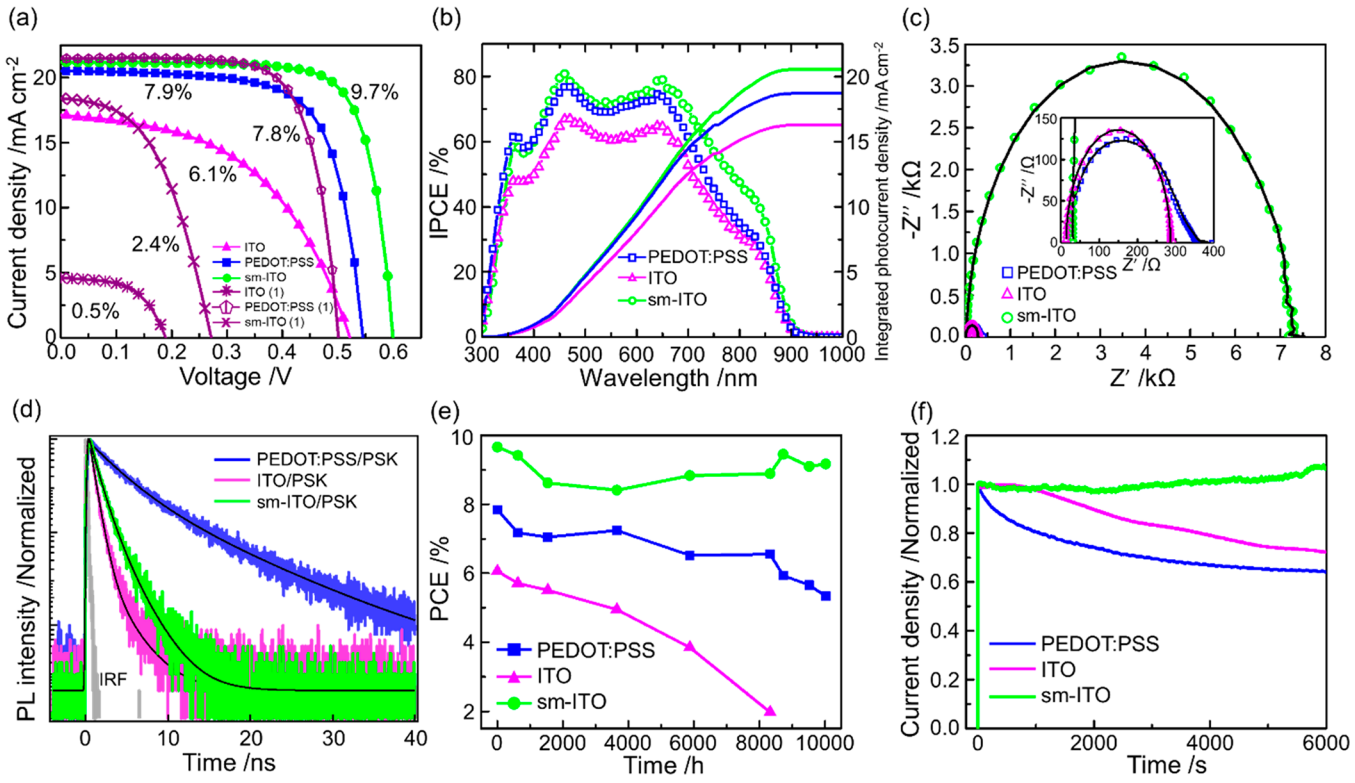

Figure 2. (a) $J-V$ characteristics and (b) the corresponding IPCE spectra of the best-performing cells. (c) EIS spectra (inset shows the lack of additional semicircle at the high frequency region associated with charge transfer resistance). (d) PL transients of the perovskite samples prepared on PEDOT:PSS, bare ITO, and sm-ITO electrodes. (e) Evolution in the PCE of the champion cells in each category in an unencapsulated condition showing the long-term stability as a function of storage period inside a nitrogen-filled glovebox. (f) Normalized current density recorded from the devices under simulated AM 1.5G illumination at the maximum power point for the unencapsulated cells under ambient conditions. The sm-ITO device shows an impressive shelf stability by retaining over 90% of the initial PCE for over 10000 h and also does not show any reduction in the current density under continuous illumination. The legends labeled (1) in Figure 2a represent the devices fabricated according to the conventional one-step approach.

higher V_O and less M−OH relative to ITO-400, which arises from nanoparticle incorporation. Owing to the presence of Sn in minor quantities, the M−O intensity can predominantly be assigned to In−O rather than Sn−O. The In 3d spectra in Figure S5c show a reduced $In(OH)_3$ peak intensity with increased In−O peak intensity for both ITO-400 and sm-ITO accounting for the dehydration of loosely bound hydroxyl groups that can induce weak interfacial charge transfer, leading to suppressed device performance.[24] Hence, this dehydration process can be expected to improve the interfacial carrier kinetics for sm-ITO. Note that while there is a similarity between ITO-400 and sm-ITO, the overall changes in the surface chemical composition became much improved for sm-ITO compared to ITO-400 with significantly reduced carbon contamination for the former (Table S1). These adjustments in the defective surface oxygen vacancies and hydroxyls associated with In lead to significant improvements in the optical transmittance of the electrodes in the long-wavelength region (>750 nm shown in Figure S6a) for the sm-ITO in comparison to the other subtrates,[39] which is highly desired for narrow-bandgap semiconductors like tin perovskites to improve the light-harvesting ability. The absorption spectra obtained from ITO/PSK and sm-ITO/PSK display band edge positions almost identical to those of the PEDOT:PSS-based film (Figure S6b), implying a negligible impact on the energy band gap upon removing the underlying PEDOT:PSS layer. This was also ascertained by the normalized steady-state PL peak maxima located at the same position (~878 nm). Note that although the transmittance in the low-wavelength region (<500 nm) was slightly lower for the sm-ITO substrate in comparison to that for bare ITO, the absorbance of the corresponding perovskite sample was compensated by the better crystallinity for sm-ITO/PSK than for ITO/PSK as shown by the XRD patterns (Figure S7).

The minimal influence on the band edge upon removal of PEDOT:PSS motivated the device fabrication process. Accordingly, about 20 devices were fabricated under the same experimental conditions based on pristine ITO, ITO/PEDOT:PSS, and sm-ITO substrates (the corresponding photovoltaic parameters are given in Tables S2−S4). The box plots of the device parameters in Figure S8 show a subtle increase in overall short-circuit current density (J_{sc}) for the sm-ITO device than for the devices with PEDOT:PSS as an HTM, while the increment is quite significant when compared to bare ITO-based devices due to insufficient diffusion length of the minority carriers in the latter.[40,41] On the other hand, the open-circuit voltage (V_{oc}) distribution for sm-ITO-based devices is comparable to the range seen in the devices with PEDOT:PSS, most likely due to the interfacial modification that averts the undesired recombination routes, which is lacking in bare ITO-based devices. The same also optimizes the parasitic resistances associated with the sm-ITO devices which lead to a better fill factor (FF) that in turn gives rise to an excellent distribution in PCE in comparison to both the

https://doi.org/10.1021/acsami.3c10268
ACS Appl. Mater. Interfaces 2023, 15, 40700−40708

devices with and without PEDOT:PSS. The $J-V$ characteristics of the best-performing cells are displayed in Figure 2a, and the corresponding parameters are given in Table 1. With

Table 1. Photovoltaic Parameters for Fresh Devices Obtained under One-Sun Simulated AM 1.5G Illumination (100 mW cm^{-2}) with a Device Active Area of 0.0225 cm^2

device	J_{sc}/mA cm^{-2}	V_{oc}/V	FF	PCE/%
PEDOT:PSS	20.55	0.553	0.691	7.9
ITO	17.08	0.518	0.685	6.1
sm-ITO	21.18	0.604	0.755	9.7

the highest J_{sc} of 21.18 mA cm^{-2}, V_{oc} of 0.604 V, and FF of 0.755, the sm-ITO-based device displays an outstanding PCE of 9.7%, which is much better than those of the PEDOT:PSS-based device (PCE = 7.9%) and pristine ITO-based device (PCE 6.1%). The $J-V$ characteristic curves from the devices fabricated by adopting the traditional one-step approach,[6] using bare ITO, with and without PEDOT:PSS as an HTM, and sm-ITO are also shown in Figure 2a for comparison. The bare ITO device shows a very poor performance (PCE 0.5%), while the sm-ITO device suffered from a very low V_{oc} of 0.27 V leading to a low PCE of 2.4% as a result of weak interfacial characteristics, which is overcome in the two-step approach, as it enabled stronger interfacial interaction between the perovskite and the underlying ITO electrodes, making this an indispensable approach for fabricating HTM-free solar cells with superior performance. Note that the one-step device based on PEDOT:PSS can perform as good as the device fabricated using the two-step approach. Nevertheless, it still suffers from a relatively lower V_{oc} (~0.5 V) with poorer overall device performance than that of the sm-ITO device.

The IPCE spectra shown in Figure 2b support the authenticity of the $J-V$ measurements. The significantly improved EQE values of the sm-ITO device in the short-wavelength region in comparison to the pristine ITO-based device result from the suppression of electron traps for the former,[42] while the enhancement observed in the long-wavelength region results from the efficient interfacial charge collection at the ITO/PSK interface region, accounting for the overall reduced recombination losses.[43] On the whole, the charge extraction is greatly improved when sm-ITO was used. The good interfacial features in the sm-ITO device lead to its improved V_{oc} in comparison to the bare ITO device. This was also confirmed by UPS measurements (Figure S9), according to which the work function of bare (UVO-treated) ITO[44] changes from 4.68 to 4.95 eV for sm-ITO that lies much closer to the valence band maximum of PSK (−5.02 eV). While an upward band bending could occur after interface formation between ITO and PSK to facilitate hole hopping,[28] the pursued surface treatment has reduced the hole injection barrier significantly, thereby improving the V_{oc} for the sm-ITO device. Note that the surface modification led to significant reduction in the surface carbon species on the sm-ITO as discussed earlier (Table S1), which ensures a downward shift in the Fermi level of sm-ITO and increased the work function, making it more convenient for hole injection from the VBM of the perovskite.[45] Although this alteration in work function is possible in traditionally applied UV−ozone or oxygen plasma treatment, the resulting effect can decrease quickly with time, rendering the approach unsuitable for long-term usage. This surface instability of ITO substrates is a result of reorganization of the polar groups and recontamination of the surface by hydrocarbons in the air,[46] along with possible diffusion of indium atoms.[47] It is possible that the nanoparticle deposition prior to the thermal annealing process on the ITO substrate activates the surface for the removal of carbon contamination in large excess in addition to passivating the respective sites and preventing quick recontamination, thereby providing long-term surface/interfacial stability to the sm-ITO electrode. The swift hole extraction process was further ascertained through the dark $J-V$ characteristics from the hole-dominant devices; i.e., the PSK layer was sandwiched between the electrodes along with the hole-extraction layer (ITO/PEDOT:PSS/PSK/Al, ITO/PSK/Al and sm-ITO/PSK/Al). This space-charge-limited current measurement is highly sensitive to any modulation in the contact barrier brought about by the interfacial changes.[48,49] Figure S10 displays rapid dark current injection to perovskites from ITO and sm-ITO in comparison to the device with PEDOT:PSS as an HTM.

This larger dark current density facilitated by greater hole mobility in the sm-ITO device endorses the UPS measurements, suggesting a reduced hole-injection barrier between sm-ITO and PSK. The interfacial carrier transport in the full cell was investigated through electrochemical impedance spectroscopy (EIS) by biasing at the open-circuit voltage under darkness. The obtained Nyquist plots (Figure 2c) were fitted using an appropriate ladder-type equivalent-circuit model.[50,51] The single large semicircle in the spectra has been assigned to the recombination resistance due to the lack of additional arcs at the high-frequency region that generally represents the interfacial charge transfer resistance.[52] Further, the characteristics associated with mesoporous interlayers are missing at the low-frequency region in the sm-ITO device. On the whole, the sm-ITO device displays a significantly greater resistance against charge recombination (Table S5) due to the outstanding interfacial engineering alongside the reduced carrier traps, giving the enhanced V_{oc}. The inset in Figure 2c also shows that the PEDOT:PSS-based device suffers from significant charge recombination when compared to the sm-ITO device, while somehow, the effect is comparable to that in the device fabricated directly using bare ITO. This change could, in turn, be credited to the ITO-nanoparticle treatment toward retarded charge recombination. The series resistance of the sm-ITO device was slightly higher than those of the other two devices due to the effect of thermal annealing of the former electrode.

By fabricating a device using ITO-400, we obtained a very low PCE of 4.2% (Figure S11a), due to its poor J_{sc}. We ascribe this to the absence of interfacial modifiers like conventional HTMs[21,23] or buffer layers like self-assembled monolayers,[24,25] which enable pinhole- and defect-free perovskite layer formation leading to enhanced photocurrent generation. Similarly, the impact of the ITO nanoparticle concentration was tested by doubling it to a concentration of 10 mg mL^{-1}. Figure S11b shows a slightly increased V_{oc} with reduced J_{sc} for the double-concentrated sm-ITO device in comparison to the reported sm-ITO device, yielding a relatively poorer PCE (7.6%). This reduced J_{sc} could possibly result from the electrode characteristic, rather than the active layer itself as usually seen in mesoscopic devices with thicker mesoporous layer in a p-i-n configuration.[42] We also observed a slightly pronounced hysteresis with the device made using a doubled nanoparticle solution concentration. In contrast, the sm-ITO-based device displays negligible hysteresis as shown in Figure S12, implying the minimal impact of ion migration/interfacial

https://doi.org/10.1021/acsami.3c10268
ACS Appl. Mater. Interfaces 2023, 15, 40700−40708

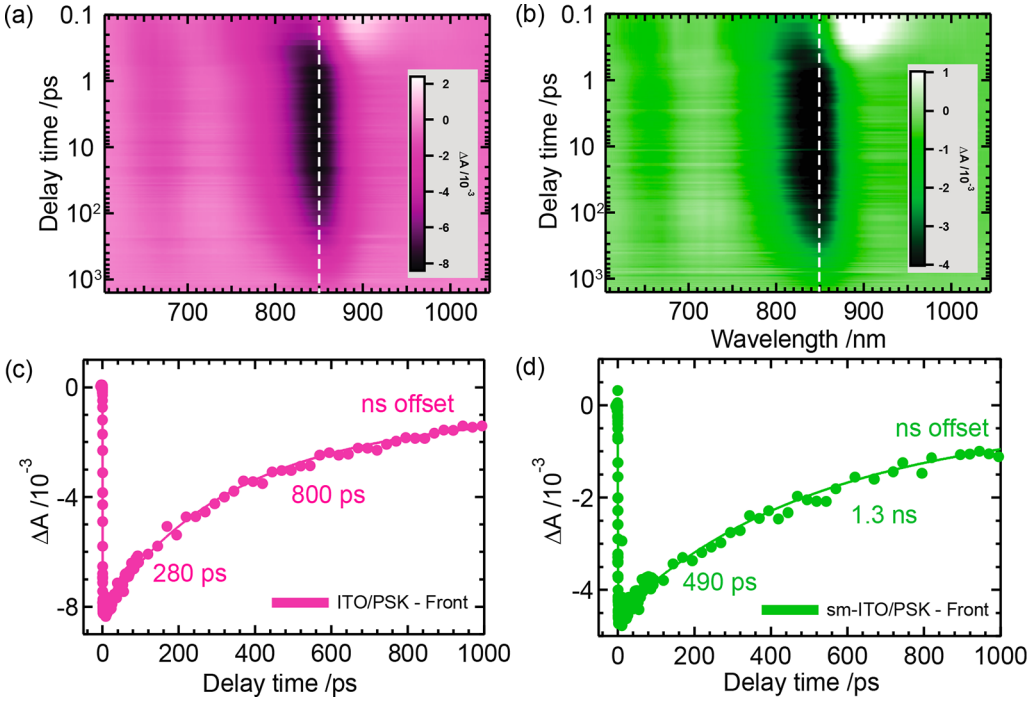

Figure 3. Femtosecond transient absorption spectrograms of the (a) ITO/PSK and (b) sm-ITO/PSK samples via excitation from the front (ITO) side. The corresponding transient kinetics of the photobleach band minima as indicated by the white dashed lines are shown in (c) and (d) for ITO/PSK and sm-ITO/PSK samples, respectively.

ion accumulation under fresh conditions, agreeing with the impedance spectral results.

The interfacial carrier dynamics was further investigated with time-resolved PL decay profiles using a time-correlated single-photon-counting (TCSPC) technique by exciting the perovskite samples ITO/PSK, sm-ITO/PSK, and PEDOT:PSS/PSK at 635 nm to understand the reason for the variation of the device performance (Figure 2d). The PL transients were obtained at the maximum intensity of the PL spectra for all the films, and they were expected to reveal the transport characteristics at the nanosecond scale to supplement the EIS results. The obtained PL decay profiles were fitted using a biexponential function model, and the fitting coefficients are given in Table S5. The average lifetimes were estimated to be 8.0, 1.1, and 1.7 ns for PEDOT:PSS/PSK, ITO/PSK, and sm-ITO/PSK films, respectively. When the perovskite films are prepared atop a charge extraction layer, the calculated average PL lifetimes generally reflect the agglomeration of both charge extraction effects and interfacial defect-mediated recombination. Thus, the significantly lower carrier lifetimes in ITO and sm-ITO support the excellent hole extraction against the PEDOT:PSS-based sample. However, the observed longer PL lifetime of sm-ITO compared to ITO could be due to the reduced interfacial defect mediated recombination for the former.

TPSCs using 1% $EDAI_2$ as additive in a traditional one-step fabrication with PEDOT:PSS as an HTM tends to display an impressive enduring stability of over 2000 h upon storing inside a nitrogen-filled glovebox due to the slow surface passivation effect of the additive,[6] while the device fabricated using the two-step method has been reported to be stable for over 6000 h.[23] Hence, we expected our devices to display an enduring stability of at least about 4000 h upon shelf storage in a glovebox. Interestingly, the sm-ITO device displayed an outstanding stability when stored inside a nitrogen-filled glovebox (Figure 2e). The conventional PEDOT:PSS-based device exhibited a degraded performance in terms of stability for over a duration of 1 year. In contrast, the sm-ITO device was able to retain over 90% of the initial PCE for more than 10000 h even under the unencapsulated condition, which shows its capacity to compete against the traditional HTM-based devices; this remarkable stability has never been reported elsewhere. On the other hand, the PCE of the bare ITO-based device continuously declined with time and died after 8000 h of shelf storage. We ascribe this enduring stability of the sm-ITO device to the combined effects of $EDAI_2$ and the incorporated ITO nanoparticles toward passivating both the perovskite surface and the sm-ITO electrode/PSK interface. The $J-V$ characteristic curves of the champion cells (PEDOT:PSS and sm-ITO) after a period of 1 year are shown in Figure S13. The forward and reverse scans clearly show pronounced hysteresis due to the effect of long-term aging which could lead to interfacial carrier/ion accumulation. Nevertheless, the sm-ITO device still displayed almost comparable J_{sc} and V_{oc} values in both the forward and reverse scans, for which the PEDOT:PSS-based device showed much poorer performance, possibly due to the interface passivation effect of the nanoparticle treatment for the former. The normalized current densities under one-sun illumination (~6000 s) under the simulated AM 1.5G condition at the maximum power point (Figure 2f) for the unencapsulated devices under ambient conditions show that the sm-ITO device can withstand harsh conditions in comparison to the control devices. This could once again be attributed to the interfacial engineering adopted in this study.

The long-term durability of the fabricated devices is predominantly a direct consequence of the superior interfacial characteristics. Apart from the activation and passivation effect of the ITO nanoparticle treatment toward long-term surface chemical reconfiguration of the sm-ITO as discussed through

https://doi.org/10.1021/acsami.3c10268
ACS Appl. Mater. Interfaces 2023, 15, 40700−40708

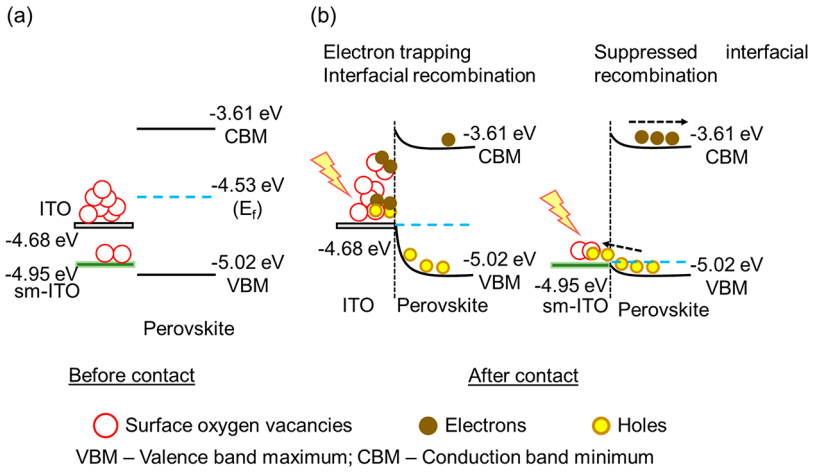

Figure 4. Mechanism illustrating the energy alignment (a) before and (b) after establishing contact between the electrodes and perovskite. According to our XPS studies, bare ITO possesses excess surface oxygen vacancies that can trap the electrons. Upon establishing an electrode/perovskite contact, while an upward band bending occurs from the perovskite VBM enabling hole hopping to the ITO, the electrons trapped by the oxygen vacancies recombine with the extracted holes at the bare ITO/perovskite interface. In contrast, the reduced oxygen vacancies in sm-ITO lead to suppressed electron traps and retarded interfacial charge recombination, while the modified work function facilitates quick hole extraction with better band alignment than that between the PSK and bare ITO.

XPS, an in-depth investigation of the charge carrier relaxation dynamics becomes essential. Hence, we performed femtosecond transient absorption spectral (TAS) studies on the PSK samples deposited on bare ITO (ITO/PSK) and sm-ITO (sm-ITO/PSK) substrates for both front (ITO side illumination) and back (PSK side illumination) excitation conditions. Figure 3 shows the front-side TAS spectrograms and the transient kinetics for the ITO/PSK and sm-ITO/PSK samples; the corresponding back-side excitation TAS data are shown in Figure S14. The TAS spectrograms of ITO/PSK and sm-ITO/PSK samples show spectral features similar to that of a PEDOT:PSS/PSK sample reported elsewhere[53] for the front-side excitation as shown in Figure 3a,b, whereas the back-side excitation produced much weaker signals with drastic changes in the spectral shapes for the ITO/PSK sample.

In contrast, the TAS spectrograms of the sm-ITO/PSK sample look similar on both front-side and back-side excitations. Furthermore, the TAS profiles at selected pump−probe delay times were taken to get a clear understanding of the differences in the spectral shapes between the front- and back-side excitations as shown in Figure S15. The ITO/PSK sample from the back-side excitation shows second-derivative shape photobleach (PB) bands with a blue shift of 10 nm compared to the front-side excitation. The blue shift of the PB band (absorption onset) is often associated with the p-doping of the valence band[54] caused by the Sn vacancies. The weaker TAS signal for the backside excitation of the ITO/PSK sample could be attributed to parasitic absorption losses caused by defects or poor quality of the nanocrystal surfaces. Unlike the ITO/PSK sample, the TAS profiles of the sm-ITO/PSK sample show PB bands with similar peak positions and magnitudes irrespective of the direction of excitation. The magnitude of second-derivative shapes of the PB bands in the sm-ITO/PSK sample are also smaller for back-side excitation, indicating reduced surface roughness when compared to the ITO/PSK sample. In summary, the TAS profiles obtained from both the front- and back-side excitations signify the higher film quality of the PSK films grown on the sm-ITO surface with slower charge recombination compared with the bare-ITO surface (Figure 3).

The TAS kinetic profiles of the PB band minima were compared between the ITO/PSK and sm-ITO/PSK samples with front-side excitation, as shown in Figure 3c,d. The TAS kinetic profiles were fitted to account for the shallow and deep trap-mediated nonradiative recombination processes.[53] The fitting coefficients of both deep (τ_1) and shallow (τ_2) trap-mediated nonradiative recombination processes for sm-ITO/PSK are retarded in comparison to those of the ITO/PSK sample, as summarized in Table S6. The shallow traps are responsible for the poor crystal quality of Sn PSK films grown on bare ITO. Theoretical calculations[4] suggest that the Sn vacancies are responsible for shallow trap state formation in Sn perovskite due to their lower formation energies. The increased oxygen vacancies in the bare ITO substrate should be responsible for the formation of Sn vacancies in the bulk state that lead to poor PSK film surface quality.

Despite the superior crystal quality and interfacial kinetics for the sm-ITO/PSK sample over bare ITO/PSK, back-side excitation produced accelerated decay from deep trap states formed on the top surface of nanocrystals. According to the theoretical calculations,[4] deep trap states are predominantly formed due to interstitial type defects. To further improve the photovoltaic performance, it is necessary to overcome the deep trap defect formation in Sn perovskite samples in addition to reducing the most common Sn vacancy formation. Altogether, the superior carrier extraction ability of PSK films developed over sm-ITO relative to the bare ITO can be attributed to the better perovskite film formation due to the nanoparticle treatment that suppressed the defective ITO oxygen vacancies, strengthened the stable In−O bonding, and got rid of excess surface carbon contamination, leading to a much more appropriate band alignment as envisioned through the schematic demonstration shown in Figure 4. As shown in Figure 4b, excess defective oxygen vacancies in the bare ITO layer may trap the photogenerated electrons from the conduction band of PSK, leading to undesirable charge recombination with the holes coming from the valence band. This interfacial charge recombination would lead to performance degradation for the bare ITO device. In contrast, when these traps are removed, this interfacial charge recombination

https://doi.org/10.1021/acsami.3c10268
ACS Appl. Mater. Interfaces 2023, 15, 40700−40708

is suppressed, leading to the outstanding performance and stability as reported in the sm-ITO device.

CONCLUSION

We have successfully fabricated HTM-free TPSCs by facile ITO nanoparticle treatment over ITO glass, followed by a two-step thermal treatment to tailor the surface properties of the ITO electrode. The surface-modified ITO (sm-ITO) electrodes displayed broad-band transmittance allowed by repaired oxygen vacancies and improved surface metal−oxygen bonding and possessed the appropriate work function that aligned well with the valence band maximum of the perovskite for swift hole extraction. The modulated electrode work function results mainly from the surface chemical reconfiguration of sm-ITO facilitated by nanoparticle treatment. The XPS results suggested that the excess carbon contamination was significantly reduced in sm-ITO, and we report that the nanoparticle treatment activates the ITO surface for the removal of carbon in excess quantity, while the thermal treatment eliminates them. Further, the nanoparticles passivate the carbon-removed sites so as to prevent rapid recontamination of the substrate. Consequently, the devices fabricated by using the sm-ITO yielded an outstanding PCE of 9.7%, which is much greater than those of the PEDOT:PSS- and bare-ITO-based TPSCs. Furthermore, due to the outstanding interfacial properties, the sm-ITO devices also exhibited a long-term stability by retaining over 90% of its initial PCE upon shelf storage in a glovebox for a period of over 10000 h, which is unprecedented for an unencapsulated TPSC. The retarded interfacial charge recombination and the superior carrier transport kinetics were assessed by using EIS, TCSPC, and TAS techniques, and the results endorse the discussed device characteristics. This work thus promotes a promising research direction toward eliminating HTMs to attain great device performance and stability for future scaling-up development.

EXPERIMENTAL SECTION

Materials. SnI_2 (99.999%, Aldrich), SnF_2 (99%, Aldrich), $EDAI_2$ (Greatcell Solar), FAI (Greatcell Solar), DMSO (Aldrich), chlorobenzene (CB, 99.8% anhydrous, Aldrich), isopropyl alcohol (IPA, 99.5% anhydrous, Aldrich), 1,1,1,3,3,3-hexafluoro-2-propanol (HFP) (>99%, TCI), ITO nanoparticles (In_2O_3:SnO_2 = 90:10, 99.99%, 20−70 nm, US Research Nanomaterials Inc.), 2,9-dimethyl-4,7-diphenyl-1,10-phenanthroline (BCP), and fullerene (C_{60}) were used as received. Dried ethanol was prepared by distillation to disperse the ITO nanoparticles.

Thin-Film and Device Fabrication. Commercially available ITO glass substrates (1.9 × 1.9 cm^2) were washed, oven-dried, and subjected to UV−ozone (UVO) for 20 min. ITO nanoparticles (5 mg) were dispersed well in 1 mL of dried ethanol via ultrasonication. The homogeneous solution was filtered thereafter and spin-coated onto the ITO substrates (5000 rpm, 50 s), and the substrates were transferred to a muffle furnace for a two-step sintering process (100 °C for 10 min, 400 °C for 30 min). After cooling, the substrates were subjected to UVO for another 20 min to obtain the surface-modified ITO (sm-ITO) electrodes. Eventually, they were moved to a nitrogen-filled glovebox (O_2 ≤2 ppm; H_2O ≤0.5 ppm) for perovskite (PSK) deposition. A reference PEDOT:PSS, as a hole transport material (HTM), was spin-coated (5000 rpm for 50 s) onto the ITO substrates after UVO treatment (20 min), followed by annealing at 150 °C for 10 min on a hot plate, to use as a standard control experiment. In addition, UVO-treated (20 min) ITO glass substrates were directly employed for perovskite deposition for performance comparison.

Preparation of perovskite ink was undertaken in a nitrogen-filled glovebox. For the two-step sequential deposition process, spin-coating the inorganic SnI_2 solution onto the substrate was the first step, while the organic FAI deposition made up the second step. For the first step, a 40 μL solution of DMSO comprising 372.5 mg of SnI_2, 31.3 mg of SnF_2, and 3.16 mg of $EDAI_2$ dissolved in 1.25 mL of DMSO was spin-coated atop UVO-treated ITO or ITO/PEDOT:PSS or sm-ITO at 6000 rpm for 60 s without annealing. For the second step, the glovebox was first purged for 10−15 min, and a 100 μL FAI solution (20 mg of FAI dissolved in a mixed solvent system composed of IPA:HFP:CB in 5:5:2 ratio) was quickly injected on top of the SnI_2/DMSO layer. After waiting 30 s, the substrates were spun at 5000 rpm for 12 s. Immediately after spin-coating, the films were annealed at 70 °C for 10 min on a hot plate. C_{60} as an electron transport layer (thickness ∼35 nm), BCP as a hole-blocking layer (thickness ∼5 nm), and silver as a metal electrode (thickness ∼100 nm) were deposited via thermal evaporation in a high-vacuum system (pressure 5 × 10^{-6} Torr).

Sample and Device Characterization. A field-emission scanning electron microscope (SEM, SU8010, Hitachi) was used to observe the surface morphology and cross-section of the substrates and the perovskite films formed over their surface. X-ray diffraction (XRD) patterns were recorded with a Bruker D8-Advance diffractometer using Cu Kα radiation. X-ray photoelectron spectra (XPS) and ultraviolet photoelectron spectra (UPS) were acquired with a Thermo K-ALPHA Surface Analyzer. The UPS spectra were calibrated based on the Fermi edge of Au to compensate for any existing mismatch, and the samples were biased at −5 V. The light transmittance and absorption spectra were recorded using a UV−visible spectrophotometer (V-780, Jasco) equipped with an integration sphere (ISN-9011, Jasco). The steady-state photoluminescence (PL) experiment was undertaken using a laboratory-built PL system, as described elsewhere.[53] For this, the perovskite samples were excited at a wavelength of 450 nm, and the emission spectra were observed between 600 and 1100 nm by blocking the scattering excitation light using a long-pass filter (650 nm) at the entrance slit of the emission monochromator. The time-resolved photoluminescene (PL) measurement was performed using a time-correlated single-photon-counting (TCSPC) system (Fluotime 200, PicoQuant) by exciting the samples at 635 nm with a picosecond pulsed-diode laser (LDH-635, PicoQuant, fwhm ∼70 ps). The femtosecond transient absorption spectroscopic experiments were performed using a CDP transient absorption pump−probe spectrometer described elsewhere.[55] The ITO/PSK and sm-ITO/PSK samples were excited using 520 nm pump pulses and probed between 650 and 1050 nm. The excitation pulse energy was set to 2 μJ cm^{-2}. For all the photophysical characterizations, the perovskite samples were prepared on UVO-treated ITO glass and sm-ITO substrate, followed by careful encapsulation with a glass substrate by applying optical adhesive (Norland 61, Thorlabs NOA61) and curing it using intense UV light illumination.

The J−V characteristics of the fabricated devices were recorded using a Keithley 2400 digital source meter under 1 sun illumination (AM 1.5G, 100 mW/cm^2) by employing a solar simulator (XES-40S1, SAN-EI) calibrated with a standard reference silicon cell (Oriel, PN 91150 V, VLSI standard). All measurements were performed under ambient conditions with voltage scan steps of 0.02 V for both reverse and forward scans. A metal mask was placed over the devices in such a way that only an area of 0.0225 cm^2 was exposed to the light during measurement. A system made of a Xe lamp (A-1010, PTi, 150 W), a monochromator (PTi), and a digital source meter (Keithley 2400) was used to record the incident photon to current conversion efficiency (IPCE) of the devices after being calibrated with a standard Si photodiode (S1337-1012BQ, Hamamatsu). Electrochemical impedance spectroscopy (EIS) was performed in darkness with an AC amplitude of 20 mV in the frequency range between 4 MHz and 1 Hz, where the devices were biased at their respective open-circuit (V_{oc}) conditions. All the device measurements were performed under ambient conditions.

https://doi.org/10.1021/acsami.3c10268
ACS Appl. Mater. Interfaces 2023, 15, 40700−40708

■ ASSOCIATED CONTENT

Supporting Information

The Supporting Information is available free of charge at https://pubs.acs.org/doi/10.1021/acsami.3c10268.

SEM, contact angles, XRD, XPS, UV−visible absorbance/PL spectra, statistics box plots of device parameters, UPS, SCLC dark $J-V$ curves, device characteristic $J-V$ curves, and femtosecond TAS spectra decay profiles (PDF)

■ AUTHOR INFORMATION

Corresponding Author

Eric Wei-Guang Diau − *Department of Applied Chemistry and Institute of Molecular Science and Center for Emergent Functional Matter Science, National Yang Ming Chiao Tung University, Hsinchu 300093, Taiwan;* orcid.org/0000-0001-6113-5679; Email: diau@nycu.edu.tw

Authors

Parameswaran Rajamanickam − *Department of Materials Science and Engineering, National Yang Ming Chiao Tung University, Hsinchu 300093, Taiwan;* orcid.org/0000-0001-9377-2963

Sudhakar Narra − *Department of Applied Chemistry and Institute of Molecular Science and Center for Emergent Functional Matter Science, National Yang Ming Chiao Tung University, Hsinchu 300093, Taiwan;* orcid.org/0000-0003-4893-9204

Ashank Seetharaman − *Department of Applied Chemistry and Institute of Molecular Science, National Yang Ming Chiao Tung University, Hsinchu 300093, Taiwan;* orcid.org/0000-0002-4417-8631

Complete contact information is available at: https://pubs.acs.org/10.1021/acsami.3c10268

Notes

The authors declare no competing financial interest.

■ ACKNOWLEDGMENTS

This work was supported by the National Science and Technology Council (Grant Nos. NSTC 111-2634-F-A49-007, NSTC 111-2123-M-A49-001, and NSTC 112-2639-M-A49-001-ASP) and Centre for Emergent Functional Matter Science of National Yang Ming Chiao Tung University (NYCU) from The Featured Areas Research Centre Program within the framework of the Higher Education Sprout Project by the Taiwan Ministry of Education (MOE).

■ REFERENCES

(1) Diau, E. W. G. Next-Generation Solar Cells and Conversion of Solar Energy. *ACS Energy Lett.* **2017**, *2* (2), 334−335.

(2) Diau, E. W. G.; Jokar, E.; Rameez, M. Strategies to Improve Performance and Stability for Tin-Based Perovskite Solar Cells. *ACS Energy Lett.* **2019**, *4*, 1930−1937.

(3) Wang, F.; Ma, J.; Xie, F.; Li, L.; Chen, J.; Fan, J.; Zhao, N. Organic Cation-Dependent Degradation Mechanism of Organotin Halide Perovskites. *Adv. Funct. Mater.* **2016**, *26* (20), 3417−3423.

(4) Shi, T.; Zhang, H. S.; Meng, W.; Teng, Q.; Liu, M.; Yang, X.; Yan, Y.; Yip, H. L.; Zhao, Y. J. Effects of Organic Cations on the Defect Physics of Tin Halide Perovskites. *J. Mater. Chem. A* **2017**, *5* (29), 15124−15129.

(5) Peng, L.; Xie, W. Theoretical and Experimental Investigations on the Bulk Photovoltaic Effect in Lead-Free Perovskites $MASnI_3$ and $FASnI_3$. *RSC Adv.* **2020**, *10* (25), 14679−14688.

(6) Jokar, E.; Chien, C. H.; Fathi, A.; Rameez, M.; Chang, Y. H.; Diau, E. W. G. Slow Surface Passivation and Crystal Relaxation with Additives to Improve Device Performance and Durability for Tin-Based Perovskite Solar Cells. *Energy Environ. Sci.* **2018**, *11* (9), 2353−2362.

(7) Jokar, E.; Chien, C. H.; Tsai, C. M.; Fathi, A.; Diau, E. W. G. Robust Tin-Based Perovskite Solar Cells with Hybrid Organic Cations to Attain Efficiency Approaching 10%. *Adv. Mater.* **2019**, *31*, 1804835.

(8) Jokar, E.; Chuang, H.; Kuan, C.; Wu, H.; Hou, C.; Shyue, J.; Diau, E. W. Slow Passivation and Inverted Hysteresis for Hybrid Tin Perovskite Solar Cells Attaining 13.5% via Sequential Deposition. *J. Phys. Chem. Lett.* **2021**, *12*, 10106−10111.

(9) Kuan, C.-H.; Chih, J.-M.; Chen, Y.-C.; Liu, B.-H.; Wang, C.-H.; Hou, C.-H.; Shyue, J.-J.; Diau, E. W.-G. Additive Engineering with Triple Cations and Bifunctional Sulfamic Acid for Tin Perovskite Solar Cells Attaining a PCE Value of 12.5% without Hysteresis. *ACS Energy Lett.* **2022**, *7*, 4436−4442.

(10) Kuan, C.; Ko, Y.; Diau, E. W. Surface and Interfacial Passivations for $FASnI_3$ Solar Cells with Co-Cations. *ACS Energy Lett.* **2023**, *8*, 2423−2425.

(11) Meng, X.; Wang, Y.; Lin, J.; Liu, X.; He, X.; Barbaud, J.; Wu, T.; Noda, T.; Yang, X.; Han, L. Surface-Controlled Oriented Growth of $FASnI_3$ Crystals for Efficient Lead-Free Perovskite Solar Cells. *Joule* **2020**, *4* (4), 902−912.

(12) Meng, X.; Lin, J.; Liu, X.; He, X.; Wang, Y.; Noda, T.; Wu, T.; Yang, X.; Han, L. Highly Stable and Efficient $FASnI_3$-Based Perovskite Solar Cells by Introducing Hydrogen Bonding. *Adv. Mater.* **2019**, *31* (42), 1903721.

(13) Liu, X.; Wang, Y.; Wu, T.; He, X.; Meng, X.; Barbaud, J.; Chen, H.; Segawa, H.; Yang, X.; Han, L. Efficient and Stable Tin Perovskite Solar Cells Enabled by Amorphous-Polycrystalline Structure. *Nat. Commun.* **2020**, *11*, 2678.

(14) Cao, D. H.; Stoumpos, C. C.; Yokoyama, T.; Logsdon, J. L.; Song, T.-B.; Farha, O. K.; Wasielewski, M. R.; Hupp, J. T.; Kanatzidis, M. G. Thin Films and Solar Cells Based on Semiconducting Two-Dimensional Ruddlesden-Popper $(CH_3(CH_2)_3NH_3)_2(CH_3NH_3)_{n-1}Sn_nI_{3n+1}$ Perovskites. *ACS Energy Lett.* **2017**, *2* (5), 982−990.

(15) Wang, F.; Jiang, X.; Chen, H.; Shang, Y.; Liu, H.; Wei, J.; Zhou, W.; He, H.; Liu, W.; Ning, Z. 2D-Quasi-2D-3D Hierarchy Structure for Tin Perovskite Solar Cells with Enhanced Efficiency and Stability. *Joule* **2018**, *2* (12), 2732−2743.

(16) Jiang, X.; Wang, F.; Wei, Q.; Li, H.; Shang, Y.; Zhou, W.; Wang, C.; Cheng, P.; Chen, Q.; Chen, L.; Ning, Z. Ultra-High Open-Circuit Voltage of Tin Perovskite Solar Cells via an Electron Transporting Layer Design. *Nat. Commun.* **2020**, *11*, 1245.

(17) Jokar, E.; Cheng, P. Y.; Lin, C. Y.; Narra, S.; Shahbazi, S.; Wei-Guang Diau, E. Enhanced Performance and Stability of 3D/2D Tin Perovskite Solar Cells Fabricated with a Sequential Solution Deposition. *ACS Energy Lett.* **2021**, *6* (2), 485−492.

(18) Yu, B.-B.; Chen, Z.; Zhu, Y.; Wang, Y.; Han, B.; Chen, G.; Zhang, X.; Du, Z.; He, Z. Heterogeneous 2D/3D Tin-Halides Perovskite Solar Cells with Certified Conversion Efficiency Breaking 14%. *Adv. Mater.* **2021**, *33* (36), 2102055.

(19) Wang, C.; Zhang, Y.; Gu, F.; Zhao, Z.; Li, H.; Jiang, H.; Bian, Z.; Liu, Z. Illumination Durability and High-Efficiency Sn-Based Perovskite Solar Cell under Coordinated Control of Phenylhydrazine and Halogen Ions. *Matter* **2021**, *4* (2), 709−721.

(20) Cameron, J.; Skabara, P. J. The Damaging Effects of the Acidity in PEDOT:PSS on Semiconductor Device Performance and Solutions Based on Non-Acidic Alternatives. *Mater. Horizons* **2020**, *7* (7), 1759−1772.

(21) Kuan, C.-H.; Luo, G.-S.; Narra, S.; Maity, S.; Hiramatsu, H.; Tsai, Y.-W.; Lin, J.-M.; Hou, C.-H.; Shyue, J.-J.; Diau, E. W.-G. How Can a Hydrophobic Polymer Ptaa Serve as a Hole- Transport Layer

for an Inverted Tin Perovskite Solar Cell? *Chem. Eng.* **2022**, *450* (P2), 138037.
(22) Rombach, F. M.; Haque, S. A.; Macdonald, T. J. Lessons Learned from Spiro-OMeTAD and PTAA in Perovskite Solar Cells. *Energy Environ. Sci.* **2021**, *14* (10), 5161−5190.
(23) Kuan, C.; Balasaravanan, R.; Hsu, S.; Ni, J.; Tsai, Y.; Zhang, Z.; Chen, M.; Diau, E. W. Dopant-Free Pyrrolopyrrole-Based (PPr) Polymeric Hole-Transporting Materials for Efficient Tin-Based Perovskite Solar Cells with Stability Over 6000 h. *Adv. Mater.* **2023**, *35*, 2300681.
(24) Song, D.; Narra, S.; Li, M. Y.; Lin, J. S.; Diau, E. W. G. Interfacial Engineering with a Hole-Selective Self-Assembled Monolayer for Tin Perovskite Solar Cells via a Two-Step Fabrication. *ACS Energy Lett.* **2021**, *6* (12), 4179−4186.
(25) Afraj, S. N.; Kuan, C. H.; Lin, J. S.; Ni, J. S.; Velusamy, A.; Chen, M. C.; Diau, E. W. G. Quinoxaline-Based X-Shaped Sensitizers as Self-Assembled Monolayer for Tin Perovskite Solar Cells. *Adv. Funct. Mater.* **2023**, *33*, 2213939.
(26) Marshall, K. P.; Walker, M.; Walton, R. I.; Hatton, R. A. Enhanced Stability and Efficiency in Hole-Transport-Layer-Free $CsSnI_3$ Perovskite Photovoltaics. *Nat. Energy* **2016**, *1*, 16178.
(27) Lin, J. T.; Chu, T. C.; Chen, D. G.; Huang, Z. X.; Chen, H. C.; Li, C. S.; Wu, C. I.; Chou, P. T.; Chiu, C. W.; Chen, H. M. Vertical 2D/3D Heterojunction of Tin Perovskites for Highly Efficient HTM-Free Perovskite Solar Cell. *ACS Appl. Energy Mater.* **2021**, *4* (3), 2041−2048.
(28) Liu, X.; Wu, T.; Zhang, C.; Zhang, Y.; Segawa, H.; Han, L. Interface Energy-Level Management toward Efficient Tin Perovskite Solar Cells with Hole-Transport-Layer-Free Structure. *Adv. Funct. Mater.* **2021**, *31*, 2106560.
(29) Hotchkiss, P. J.; Jones, S. C.; Paniagua, S. A.; Sharma, A.; Kippelen, B.; Armstrong, N. R.; Marder, S. R. The Modification of Indium Tin Oxide with Phosphonic Acids: Mechanism of Binding, Tuning of Surface Properties, and Potential for Use in Organic Electronic Applications. *Acc. Chem. Res.* **2012**, *45* (3), 337−346.
(30) Abd-Elnaiem, A. M.; Hakamy, A. Influence of Annealing Temperature on Structural, Electrical, and Optical Properties of 80 Nm Thick Indium-Doped Tin Oxide on Borofloat Glass. *J. Mater. Sci. Mater. Electron.* **2022**, *33* (30), 23293−23305.
(31) Kim, J. S.; Friend, R. H.; Cacialli, F. Surface Energy and Polarity of Treated Indium-Tin-Oxide Anodes for Polymer Light-Emitting Diodes Studied by Contact-Angle Measurements. *J. Appl. Phys.* **1999**, *86* (5), 2774−2778.
(32) Kim, J. S.; Friend, R. H.; Cacialli, F. Improved Operational Stability of Polyfluorene-Based Organic Light-Emitting Diodes with Plasma-Treated Indium-Tin-Oxide Anodes. *Appl. Phys. Lett.* **1999**, *74* (21), 3084−3086.
(33) Shahbazi, S.; Li, M. Y.; Fathi, A.; Diau, E. W. G. Realizing a Cosolvent System for Stable Tin-Based Perovskite Solar Cells Using a Two-Step Deposition Approach. *ACS Energy Lett.* **2020**, *5* (8), 2508−2511.
(34) Liu, X.; Yan, K.; Tan, D.; Liang, X.; Zhang, H.; Huang, W. Solvent Engineering Improves Efficiency of Lead-Free Tin-Based Hybrid Perovskite Solar Cells beyond 9%. *ACS Energy Lett.* **2018**, *3* (11), 2701−2707.
(35) Biesinger, M. C. Accessing the Robustness of Adventitious Carbon for Charge Referencing (Correction) Purposes in XPS Analysis: Insights from a Multi-User Facility Data Review. *Appl. Surf. Sci.* **2022**, *597* (May), 153681.
(36) Yahya, M.; Fadavieslam, M. R. Effect of Oxygen Plasma on ITO Surface and OLED Physical Properties. *Microelectron. Reliab.* **2023**, *144* (March), 114981.
(37) Donley, C.; Dunphy, D.; Paine, D.; Carter, C.; Nebesny, K.; Lee, P.; Alloway, D.; Armstrong, N. R. Characterization of Indium-Tin Oxide Interfaces Using X-Ray Photoelectron Spectroscopy and Redox Processes of a Chemisorbed Probe Molecule: Effect of Surface Pretreatment Conditions. *Langmuir* **2002**, *18* (2), 450−457.
(38) Gonçalves, G.; Elangovan, E.; Barquinha, P.; Pereira, L.; Martins, R.; Fortunato, E. Influence of Post-Annealing Temperature on the Properties Exhibited by ITO, IZO and GZO Thin Films. *Thin Solid Films* **2007**, *515* (24), 8562−8566.
(39) Ren, Y.; Liu, P.; Liu, R.; Wang, Y.; Wei, Y.; Jin, L.; Zhao, G. The Key of ITO Films with High Transparency and Conductivity: Grain Size and Surface Chemical Composition. *J. Alloys Compd.* **2022**, *893*, 162304.
(40) Bretschneider, S. A.; Weickert, J.; Dorman, J. A.; Schmidt-Mende, L. Research Update: Physical and Electrical Characteristics of Lead Halide Perovskites for Solar Cell Applications. *APL Mater.* **2014**, *2* (4), 040701.
(41) Gevorkian, Z.; Gasparian, V.; Lozovik, Y. Large Diffusion Lengths of Excitons in Perovskite and TiO_2 Heterojunction. *Appl. Phys. Lett.* **2016**, *108* (5), 051109.
(42) Ramirez, D.; Schutt, K.; Montoya, J. F.; Mesa, S.; Lim, J.; Snaith, H. J.; Jaramillo, F. Meso-Superstructured Perovskite Solar Cells: Revealing the Role of the Mesoporous Layer. *J. Phys. Chem. C* **2018**, *122* (37), 21239−21247.
(43) Nakane, A.; Tampo, H.; Tamakoshi, M.; Fujimoto, S.; Kim, K. M.; Kim, S.; Shibata, H.; Niki, S.; Fujiwara, H. Quantitative Determination of Optical and Recombination Losses in Thin-Film Photovoltaic Devices Based on External Quantum Efficiency Analysis. *J. Appl. Phys.* **2016**, *120* (6), 064505.
(44) Song, D.; Hsu, L. Y.; Tseng, C. M.; Diau, E. W. G. Solution-Processed ITO Nanoparticles as Hole-Selective Electrodes for Mesoscopic Lead-Free Perovskite Solar Cells. *Mater. Adv.* **2021**, *2* (2), 754−759.
(45) Fang, M.; Zhang, C.; Chen, Q. Tuning the ITO Work Function by Capacitively Coupled Plasma and Its Application in Inverted Organic Solar Cells. *Appl. Surf. Sci.* **2016**, *385*, 28−33.
(46) You, Z. Z. Combined AFM, XPS, and Contact Angle Studies on Treated Indium-Tin-Oxide Films for Organic Light-Emitting Devices. *Mater. Lett.* **2007**, *61* (18), 3809−3814.
(47) He, K.; Yang, X.; Yan, H.; Wu, Z.; Li, Z.; Zhong, S.; Ou, Q.; Liang, R. Work Function Changes of Plasma Treated Indium Tin Oxide. *Org. Electron.* **2014**, *15* (8), 1731−1737.
(48) Kong, W.; Li, W.; Liu, C.; Liu, H.; Miao, J.; Wang, W.; Chen, S.; Hu, M.; Li, D.; Amini, A.; Yang, S.; Wang, J.; Xu, B.; Cheng, C. Organic Monomolecular Layers Enable Energy-Level Matching for Efficient Hole Transporting Layer Free Inverted Perovskite Solar Cells. *ACS Nano* **2019**, *13* (2), 1625−1634.
(49) Sajedi Alvar, M.; Blom, P. W. M.; Wetzelaer, G. J. A. H. Space-Charge-Limited Electron and Hole Currents in Hybrid Organic-Inorganic Perovskites. *Nat. Commun.* **2020**, *11* (1), 4023.
(50) Von Hauff, E. Impedance Spectroscopy for Emerging Photovoltaics. *J. Phys. Chem. C* **2019**, *123* (18), 11329−11346.
(51) Abdulrahim, S. M.; Ahmad, Z.; Bahadra, J.; Al-Thani, N. J. Electrochemical Impedance Spectroscopy Analysis of Hole Transporting Material Free Mesoporous and Planar Perovskite Solar Cells. *Nanomaterials* **2020**, *10* (9), 1635.
(52) Tsai, C. M.; Mohanta, N.; Wang, C. Y.; Lin, Y. P.; Yang, Y. W.; Wang, C. L.; Hung, C. H.; Diau, E. W. G. Formation of Stable Tin Perovskites Co-Crystallized with Three Halides for Carbon-Based Mesoscopic Lead-Free Perovskite Solar Cells. *Angew. Chemie - Int. Ed.* **2017**, *56* (44), 13819−13823.
(53) Narra, S.; Jokar, E.; Pearce, O.; Lin, C.; Fathi, A.; Diau, E. W. Femtosecond Transient Absorption Spectra and Dynamics of Carrier Relaxation of Tin Perovskites in the Absence and Presence of Additives. *J. Phys. Chem. Lett.* **2020**, *11*, 5699−5704.
(54) Milot, R. L.; Klug, M. T.; Davies, C. L.; Wang, Z.; Kraus, H.; Snaith, H. J.; Johnston, M. B.; Herz, L. M. The Effects of Doping Density and Temperature on the Optoelectronic Properties of Formamidinium Tin Triiodide Thin Films. *Adv. Mater.* **2018**, *30* (44), 1804506.
(55) Chang, C. W.; Chou, C. K.; Chang, I. J.; Lee, Y. P.; Diau, E. W. G. Relaxation Dynamics of Ruthenium Complexes in Solution, PMMA and TiO_2 Films: The Roles of Self-Quenching and Interfacial Electron Transfer. *J. Phys. Chem. C* **2007**, *111* (35), 13288−13296.

https://doi.org/10.1021/acsami.3c10268
ACS Appl. Mater. Interfaces 2023, 15, 40700−40708